Pure Appl. Chem., Vol. 81, No. 12, pp. 2355–2367, 2009.
doi:10.1351/PAC-CON-08-11-24

Controlled growth of $BaMoO_4$ hierarchical superstructures in functionalized ionic liquids*

Zhijun Luo[1,2], Huaming Li[2,‡], Sheng Yin[2], Jingtong Zhang[2], Kun Wang[2], Leigang Wang[1], and Qingfeng Guan[1]

[1]School of Materials Science and Engineering, Jiangsu University, Zhenjiang, 212013, China; [2]School of Chemistry and Chemical Engineering, Jiangsu University, Zhenjiang, 212013, China

Abstract: Dual-functionalized ionic liquids (ILs) containing both functionalized cation and anion offer scope for tuning of nucleation and growth steps to achieve crystallographic control. $BaMoO_4$ crystals synthesized in alkyl methylimidazolium trifluoroacetate ([$C_n$mim]TA, n = 4, 8, 16) aqueous solution display the similar shuttle-like shape. The size of building blocks assembling into the hierarchical architectures has been influenced by the inhibiting effect of the imidazolium substituent alkyl chain. With the increase of imidazolium substituent alkyl chain length, the building blocks change from the truncated octahedron to the nanosheet. The single-crystalline $BaMoO_4$ dendrites were prepared under the direction of [Omim]TA via the oriented attachment mechanism. $BaMoO_4$ porous structures have been successfully synthesized in the [Omim]TA aqueous solution via the manipulation of the growth kinetics. Whether the resultant holes in the $BaMoO_4$ structure are open or clogged depends upon variations in the molar ratio [Ba^{2+}]/[$Mo_7O_{24}^{6-}$]. Shuttle-like $BaMoO_4$ crystals made of nanosheets with the helical growth features have been successfully synthesized in the presence of [C_{16}mim]TA. In addition, the amount of [C_{16}mim]TA in the solution profoundly influences the morphology and size of the as-obtained products.

Keywords: crystal growth mechanisms; ionic liquids; microwave irradiation; nanostructures; particle synthesis.

INTRODUCTION

Hierarchical superstructures constructed by micro- and nanoscale building blocks have attracted considerable attention, since the properties of micro- and nanocrystals depend not only on their composition, but also on their structure, phase, shape, size, and size distribution [1,2]. The synthesis of hierarchical superstructures is a crucial step toward realization of functional nanodevices. Therefore, considerable effort has been focused on the well-controlled synthesis of materials with complex morphologies and architectures. In order to obtain inorganic crystals with hierarchical superstructures, many methods have been employed such as electrochemical method [3], Langmuir–Blodgett technique [4], laser ablation technique [5], wet-chemical method [6–8], etc. Among these methods, the wet-chemical method was one of the most effective methods because of its variability and simplicity. However, solid-state reactions often need high temperature and rigorous reaction conditions [9]. Generally, hier-

*Paper based on a presentation at the International Symposium on Novel Materials and their Synthesis (NMS-IV) and the 18th International Symposium on Fine Chemistry and Functional Polymers (FCFP-XVIII), 15–18 October 2008, Zhenjiang, China. Other presentations are published in this issue, pp. 2253–2424.

‡Corresponding author: Tel.: + 86 511 88791800; Fax: + 86 511 88791708; E-mail: lihm@ujs.edu.cn

archical superstructures can be formed through the evolution of 0D or 1D primary crystals via the Ostwald ripening process, oriented attachment process, or both by using surfactants as direction reagent [10–14]. The evolution of crystals from 3D dendrites to 1D rods and to 0D particles with prolonged aging time also was reported [15].

Recently, ionic liquids (ILs), as environmentally benign solvent, have received much attention for organic chemical reactions, catalysis, separations, and inorganic materials synthesis. Especially, ILs have many advantages in the synthesis of inorganic materials [16]. Nanomaterials, such as metal [17,18], alloy [19], oxide [20,21], and sulfide [22,23], etc., have been synthesized in ILs. However, few reports have been reported on the synthesis of metallic salt, though Zhu and co-workers have synthesized $PbCrO_4$ and $PbCrO_5$ nanorods in IL under microwave irradiation [24]. $BaMoO_4$ with a scheelite structure is an important material in electro-optics due to its production of green luminescence and in electro-optical applications including solid-state lasers and optical fibers [25]. Various methods have been employed to synthesize metal molybdates, such as solid-state reaction, electrochemical methods, the Czochralski technique, hydrothermal method, solvothermal synthesis, and co-precipitation [26–30]. Among these methods, the surfactant-assisted wet-chemical approach is one of the effective methods for the synthesis of inorganic materials under lower temperature. However, solid-state reaction often needs high temperature and rigorous reaction conditions [31]. A variety of $BaXO_4$ (X = Mo, W) hierarchical superstructures assembled from the nanobelts and nanowires have been synthesized in a catanionic reverse-micelle system. By adjusting the anionic and catanionic surfactants mixing ratio, $BaXO_4$ (X = Mo, W) nanosheets, nanobelts, nanowire, and penniform superstructures can be easily synthesized [32,33]. Spindle arrays, bundle-like, and brush-like $BaMoO_4$ nanostructures were also obtained in reverse micelles with a solvothermal method [27]. $BaMoO_4$ nanofibers were synthesized by using CTAB (hexadecyl trimethyl ammonium bromide) as direction reagent [30]. Recently, our group also reported a facile synthesis of $BaMoO_4$ nanostructure by using PVP (polyvinylpyrrolidone) as capping reagents [34].

Microwave-assisted heating method may be in favor of the synthesis of hierarchical superstructures [22,35,36], which can provide a very fast heating rate that can promote the nucleation rate in the nucleation period. ILs are good media for absorbing microwaves, due to the fact that they own large organic cation and little inorganic anion, i.e., high polarizability. Another important property of ILs is that different ILs can be designed by introducing some special functional groups into the organic positive ions or the inorganic negative ions of IL [16,37].

Herein, we present a facile microwave-assisted method in ILs for the synthesis of $BaMoO_4$ crystals with 3D architectures, which combine the merits between microwave heating and ILs. There are two reasons why we choose the trifluoroacetate group as the anion of IL. Firstly, the water solubility of ILs with long alkyl chain is not so good, e.g., [Omim]BF_4 and [C_{16}mim]BF_4 are not water-soluble. The water solubility of the ILs can be easily manufactured according to the design of their structure. We have synthesized [Bmim]TA, [Omim]TA, [C_{16}mim]Br, and [C_{16}mim]TA, which are water-soluble ILs, by introducing the hydrophilic carboxyl functional groups into the inorganic negative ions of IL. Another reason using carboxyl is that it can adsorbs strongly on metal and crystal surfaces and significantly alters the surface properties. In addition, the crystal growth can be adjusted by the change of imidazolium substituent alkyl chain length. $BaMoO_4$ crystals with different morphologies can be controllably synthesized by the design of ILs.

EXPERIMENTAL

Chemicals and apparatus

1-octyl-3-methylimidazolium bromide ([C_{16}mim]Br), 1-butyl-3-methylimidazolium trifluoroacetate ([Bmim]TA), 1-octyl-3-methylimidazolium trifluoroacetate ([Omim]TA), and 1-hexadecyl-3-methylimidazolium trifluoroacetate ([C_{16}mim]TA) were synthesized according to the literature [38].

$(NH_4)_6Mo_7O_{24}{\cdot}2H_2O$ and $BaCl_2{\cdot}2H_2O$ were analytically pure and were purchased from Shanghai Chemical Co. Ltd. and used without further purification.

A microwave oven (SINEO MAS-I) was equipped with a magnetic stirrer and a water-cooled condenser. Temperature was controlled by automatic adjusting of infrared temperature sensor. X-ray powder diffraction (XRD) analysis was carried out on a Bruker D8 diffractometer with high-intensity Cu Kα radiation (λ = 1.54 Å). Transmission electron microscopy (TEM) images were taken with a JEOL 2100 TEM operated at 200 kV. Scanning electron microscopy (SEM) images were taken with a Hitachi S-4800 operating at 15 kV.

Synthesis of $BaMoO_4$

In a typical synthesis of $BaMoO_4$ dendritic crystals, 0.02 M $BaCl_2{\cdot}2H_2O$ aqueous solution (1 ml) was first added to IL {[Bmim]TA or [Omim]TA} (3 ml) with vigorous stirring. Thereafter, 0.02 M $(NH_4)_6Mo_7O_{24}{\cdot}4H_2O$ aqueous solution (1 ml) was added to the solution and the mixture was refluxed under microwave irradiation at 70 °C for 20 min. After cooling to room temperature, the white precipitation was collected by centrifugation, washed several times with deionized water and absolute ethanol, then dried in a vacuum oven at 50 °C for 12 h.

In a typical synthesis of $BaMoO_4$ shuttle-like crystals with helical growth features, $[C_{16}mim]TA$ (1 g) and 0.02 M $BaCl_2{\cdot}2H_2O$ aqueous solution (1 ml) were added with vigorous stirring to deionized water (6 ml) in an airproof flask, maintained at 50 °C in an oil bath. Vigorous stirring was continued for 30 min to ensure that all reagents were dispersed homogeneously. Then 0.02 M $(NH_4)_6Mo_7O_{24}{\cdot}4H_2O$ aqueous solution (1 ml) was added. The mixture was refluxed under microwave irradiation at 70 °C for 20 min. After cooling to room temperature, the white precipitation was collected by centrifugation and washed several times with deionized water and absolute ethanol. The washed precipitation was suspended in acetonitrile in a closed vessel at 70 °C for 12 h in order to remove the $[C_{16}mim]TA$. The extraction process was repeated until complete removal of the IL from the residual $BaMoO_4$. The product was then dried in a vacuum oven at 50 °C for 12 h.

RESULTS AND DISCUSSION

Figure 1 shows the chemical structure of ionic liquids. The crystal structure and phase composition of $BaMoO_4$ were characterized by using XRD. Figure 2A shows the XRD patterns of the $BaMoO_4$ crystals synthesized in different IL (a) [Bmim]TA, (b) [Omim]TA, and (c) $[C_{16}mim]TA$. The result indicate that the three samples obtained in different IL have a tetragonal unit cell (a = 5.58 Å and c = 12.82 Å). All the diffraction peaks can be indexed to the JCPDS card No. 29-0193. No impurity peaks were de-

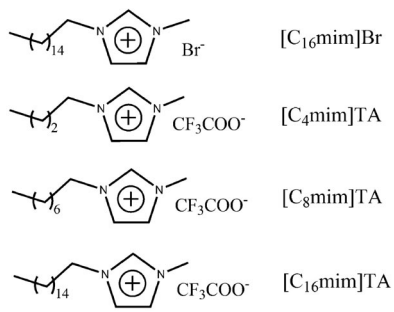

Fig. 1 Chemical structures of 1-hexadecyl-3-methylimidazolium bromide ($[C_{16}mim]Br$), 1-butyl-3-methylimidazolium trifluoroacetate ($[C_4mim]TA$), 1-octyl-3-methylimidazolium trifluoroacetate ($[C_8mim]TA$), and 1-hexadecyl-3-methylimidazolium trifluoroacetate ($[C_{16}mim]TA$).

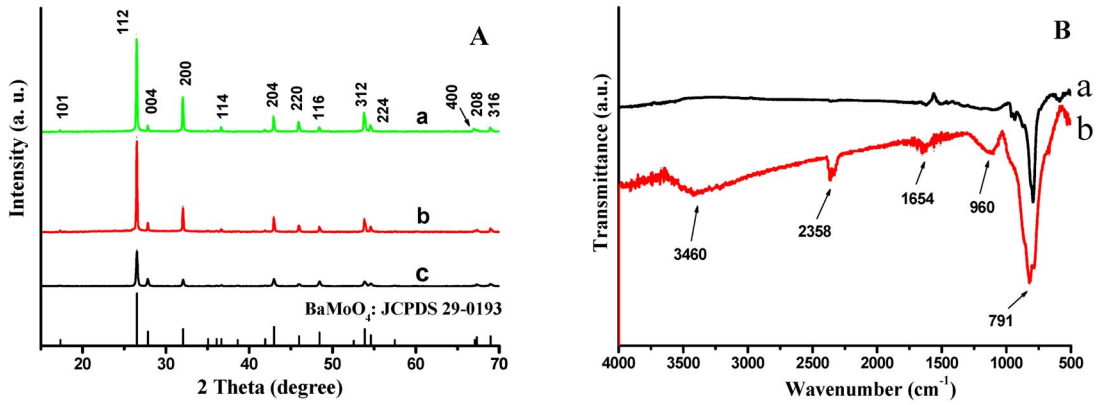

Fig. 2 A. XRD pattern of $BaMoO_4$ crystals synthesized at 70 °C in different IL aqueous solution under microwave irradiation. (a) [Bmim]TA, dendritic crystals, (b) [Omim]TA, dendritic crystals, and (c) [C_{16}mim]TA, shuttle-like crystals with helical growth features. B. FT-IR spectra of pure $BaMoO_4$ crystal (a), and $BaMoO_4$ shuttle-like crystals with helical growth features after removing the [C_{16}mim]TA (b).

tected in the experimental range. The diffraction peaks are strong and sharp, which indicates that these $BaMoO_4$ crystals with different morphologies are well crystallized.

The interaction between IL and $BaMoO_4$ crystal was investigated by the Fourier transform-infrared (FT-IR) spectra. Figure 2B shows the FT-IR spectra of pure $BaMoO_4$ crystal (a) and the $BaMoO_4$ shuttle-like crystals with helical growth features crystal synthesized by using [C_{16}mim]TA (b). The FT-IR spectra of samples a and b all show main absorption bands at ~3460, ~2358, ~1654, ~960, and ~791 cm^{-1}. Among them, the bands at ~3460 and ~2358 cm^{-1} should be corresponded to a small quantity of H_2O and CO_2. The same absorption band suggested that the interaction between [C_{16}mim]TA and $BaMoO_4$ crystal should be explained as the van der Waal attractions.

Figure 3 shows typical SEM images of the $BaMoO_4$ crystals synthesized in a reflux system at 70 °C for 20 min under microwave irradiation in the presence of [Omim]TA. The panoramic morphology (Fig. 3a) shows that the product consisted of hierarchical dendritic structure, which means that the $BaMoO_4$ with hierarchical dendritic structures can be synthesized in large scale. Higher-magnification SEM images shown in Figs. 3b,c demonstrate the detailed structural information of the sample. From Figs. 3b,c, the $BaMoO_4$ dendritic structures are constructed by a long central trunk with four 3D symmetric trunks in the middle. The long central trunk is about 10–12 μm and other four trunks in the middle are about 2–3 μm. Each trunk has one stem and four branches. The branches in each trunk are parallel to each other and in the same plane and are perpendicular to the stem. The length of branches stand on the stem becomes shorter and shorter along the top of trunk. From Fig. 3d, it can be found that the branches are rhombohedral cross-section, and the diameter of these microrods (branches) is about 250 nm. From the deep grooves between the two branches, which are shown in Fig. 3e, two rows of microtowers standing on the stem was carefully observed and revealed that the microtower consisted of linked octahedron with a truncated bottom and tip and ended with an imperfect octahedron cap.

To provide further insight into the structure of the as-prepared $BaMoO_4$ dendritic structures, individual $BaMoO_4$ crystal was analyzed by TEM as well as using SAED. A representative TEM image of dendrites is shown in Fig. 3f and the inset is the corresponding selected-area electron diffraction (SAED) pattern. The TEM image shown indicates that the dendrite indeed exhibits a symmetric structure. The SAED pattern taken along the [010] zone axis confirmed that the $BaMoO_4$ dendrite is a perfect single crystal. The SAED pattern also confirms that the long central trunk grows along the [001] direction while the four shorter trunks in the middle of central trunk grows along the [100] direction.

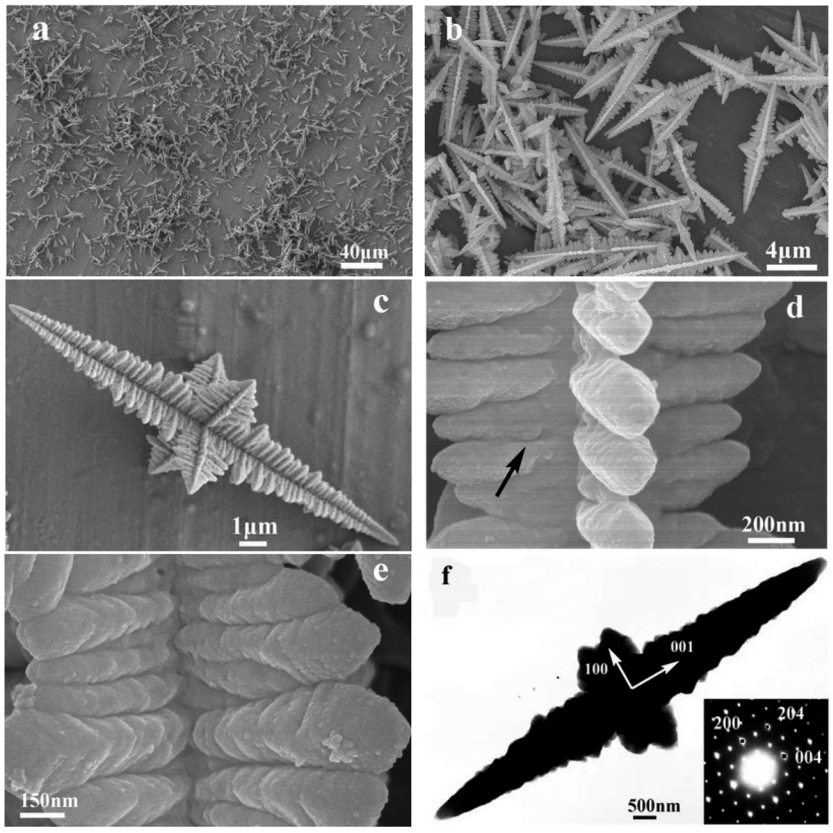

Fig. 3 SEM and TEM images of the $BaMoO_4$ dendritic crystals synthesized at 70 °C for 20 min under microwave irradiation in the presence of [Omim]TA aqueous solution, which the concentration of initial reagents $[Ba^{2+}] = [Mo_7O_{24}{}^{6-}] = 0.02$ M and the molar ratio $[Ba^{2+}]/[Mo_7O_{24}{}^{6-}] = 1$. (a) The low-magnification SEM image; (b) The high-magnification SEM image; (c–e) Different visual angle of $BaMoO_4$ dendritic crystal; (f) TEM image of individual $BaMoO_4$ dendritic crystal; the inset in Fig. 3f shows the corresponding SAED and the electron diffraction spots are marked in black dots.

To investigate the growth mechanism of $BaMoO_4$ dendritic structures, time-dependent experiments were carefully performed. The products were collected at different stages from the reaction mixture, and then the intermediate products were investigated by SEM. The rudiment of long central trunk with rough surface has already formed at room temperature before heating under microwave irradiation (Fig. 4a), which implies that the reaction is very fast. The rudimentary long central trunk was composed of a stem with four rows of many short pricks (Fig. 4a) and four protrusions in the middle of a long central trunk also burgeoned (Fig. 4b). The length of long central trunks are about 9–10 μm which are near the resultant dendrites. The rough surface of rudimentary long central trunk is made of tiny nanoparticles. It is obvious that many branches are produced through attachment of nanoparticles to the stem. With increasing the reaction time to 5 min, the main body of dendritic structure had come into being. Many nanoparticles have been found on the surface of dendritic structure which did not coalesce well to the branches or were absorbed on the surface of dendritic structure as shown by the arrows in Fig. 4c. It is obvious that the growth rate of branches far from the end of long central trunk is faster than that of the branches near the end of the long central trunk. Figure 4d is the high-magnification SEM image of area pointed by the arrow S. From the high-magnification SEM image of the end of the long central trunk (Fig. 4d), it can be found that a few nanoparticles at the tip of branches did not coalesce

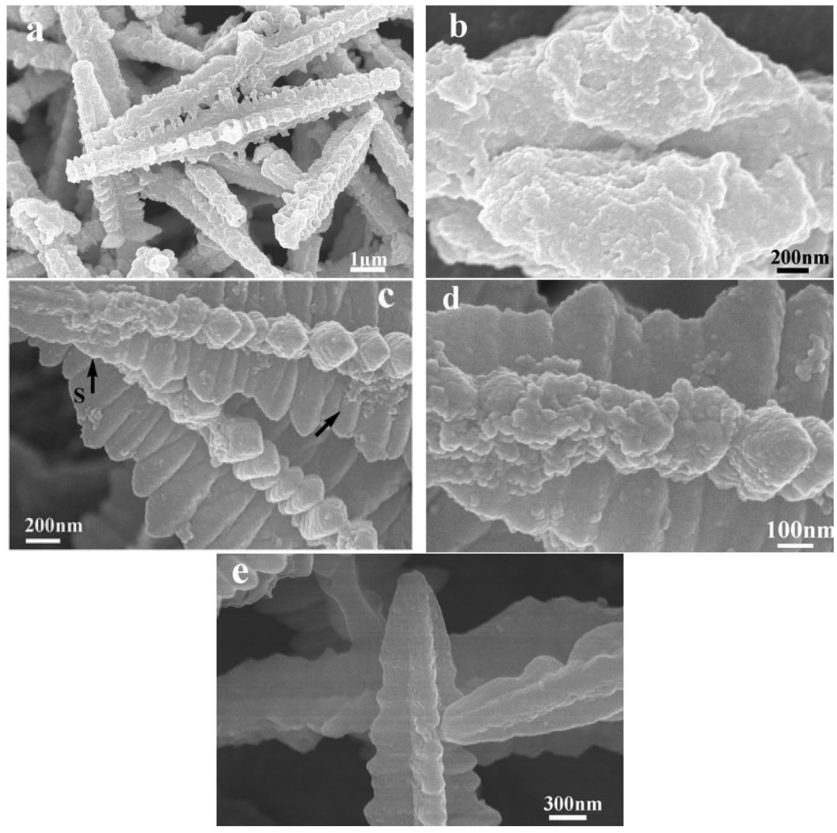

Fig. 4 SEM images of the products synthesized at 70 °C under microwave irradiation in the presence of [Omim]TA aqueous solution at different reaction time. (a) (b) Before heat under microwave irradiation; (c) (d) 5 min; (e) 20 min. Fig. 4d is the high-magnification SEM image of area pointed by the arrow S in Fig. 4c.

well to the branches. When the reaction time was increased to 20 min, few nanoparticles at the tip of the branches were found, i.e., the well-developed dendritic structures were obtained (Figs. 3c–e and 4e), which is very similar to the product obtained after heating for 5 min under microwave irradiation, suggesting that the dendritic structures essentially remained unchanged after heating for 5 min under microwave irradiation.

Nanostructure formation in a solution typically involves the fast nucleation of primary particles and the subsequent growth by two mechanisms: Ostwald ripening and oriented attachment. Ostwald ripening processes involve the growth of larger crystals at the expense of smaller crystals. Oriented attachment has been regarded as one of the important crystal growth mechanisms. The mechanism of oriented attachment refers to the attachment between two or more nanoparticles followed by sharing a common crystallographic orientation and joining at the planar interfaces. From the above experimental observations, it is reasonable that the formation of $BaMoO_4$ dendritic structures can be expressed by a two-stage growth mechanism. During Stage 1, the [001]-oriented stem has been formed under the direction of [Omim]TA in a very short time. During Stage 2, many primary nanoparticles spontaneously aggregate on the stem and further grow into [100]-oriented microtowers consisting of truncated octahedral. These primary nanoparticles with size of 30~50 nm participating in the attachment were observed on the tip of microtowers as shown in Fig. 4d. So, it is reasonable to propose that the formation of dendritic structures originates from Ostwald ripening and oriented attachment mechanisms. These primary nanoparticles as building blocks of truncated octahedral had already been formed before these

nanoparticles were coalesced into the tip of microtowers through the orientated attachment mechanism. In addition, the coalescence of dendrites in which bottlenecks between adjacent particles being filled up and surfaces of dendrites getting smoothened may attribute to the Ostwald ripening mechanisms. Similar growth process has been also observed by Cheng et al. in the synthesis of $PbMoO_4$ [13]. A reasonable growth process along [100] direction for the $BaMoO_4$ microtowers is shown in Scheme 1.

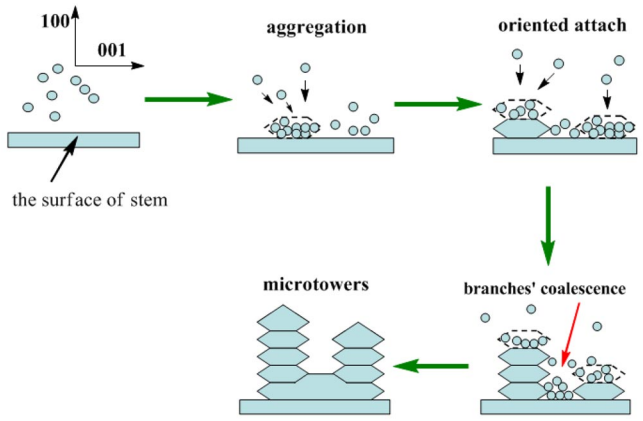

Scheme 1 Proposed growth process along the [100] direction for the $BaMoO_4$ microtowers (dendritic branches).

The penniform $BaMoO_4$ nanostructures mentioned in the introduction are similar to the dendritic structures in some ways [32]. It is noteworthy that the stems of penniform $BaMoO_4$ are grown along the [100] direction and the branches are grown along the [001] direction. However, the central stem of dendritic structures are grown along the [001] direction and the branches are grown along the [100] direction.

To investigate the effect of reaction condition on the formation of $BaMoO_4$ dendritic structures, a series of comparative experiments was carried out through similar processes. As known, the morphology of crystal does not completely depend on the thermodynamic effects because crystallization and crystal morphology often also relies on kinetic effects. Generally, the crystal growth process basically consists of a nucleation step followed by particle growth stages. The nucleation and growth stages are all supplied by the reactant species dissolved in solution. It is crucial for the formation of crystal with special morphology adjusting the kinetics growth factors.

When the molar ratio $[Ba^{2+}]/[Mo_7O_{24}{}^{6-}] = 1$, i.e., the Mo atom largely exceeds the stoichiometry, only the root area of adjacent microtowers was merged together (indicated by the black arrow in Fig. 3d). When the molar ratio $[Ba^{2+}]/[Mo_7O_{24}{}^{6-}] = 1$, the nucleation rate of $BaMoO_4$ was fast at the initial stage, due to the excess Mo atom. After the $Mo_7O_{24}{}^{6-}$ was added, large numbers of primary nanoparticles were formed, which consumed a large fraction of the reactant species in solution. $BaMoO_4$ dendritic structure can be achieved through oriented attachment of primary nanoparticles under the direction of the IL. There is not enough reactant species in solution for the subsequent coalescence of branches because the reactant species in solution has been nearly used up at the initial stage. When the molar ratio $[Ba^{2+}]/[Mo_7O_{24}{}^{6-}]$ was increased to 3, uniform shuttle-like crystals with porous surface were obtained and these shuttle-like crystals own two sharp tips and four symmetrically grown protrusions in the middle (Fig. 5a), which displayed a similar outline with the dendritic structure (shown in Fig. 3). Higher-magnification SEM images obtained from the surface of shuttle-like crystals were given in Fig. 5b, showing that many holes with size less than 100 nm in diameter located at the grooves between two neighboring branches. With the molar ratio $[Ba^{2+}]/[Mo_7O_{24}{}^{6-}]$ increased to 3, more reactant species in solution was allocated for coalescence of branches, but it is not enough for the absolute

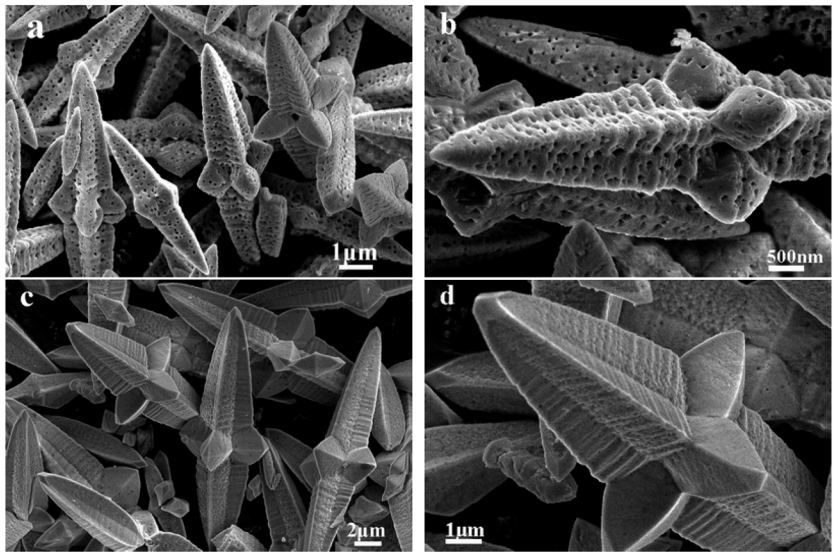

Fig. 5 SEM images of the $BaMoO_4$ shuttle-like crystals synthesized at 70 °C for 20 min under microwave irradiation in the presence of [Omim]TA aqueous solution, which the concentration of initial reagents $[Ba^{2+}] = [Mo_7O_{24}{}^{6-}] = 0.02$ M. (a) (b) the initial reagents' molar ratio $[Ba^{2+}]/[Mo_7O_{24}{}^{6-}] = 3$; (c) (d) the initial reagents' molar ratio $[Ba^{2+}]/[Mo_7O_{24}{}^{6-}] = 7$.

coalescence of branches. These holes originated from the unfinished coalescence of branches of $BaMoO_4$ dendritic structure. With the molar ratio $[Ba^{2+}]/[Mo_7O_{24}{}^{6-}]$ increased to 7, the morphology of product was similar to the product synthesized at the molar ratio $[Ba^{2+}]/[Mo_7O_{24}{}^{6-}] = 3$. However, the completion of the branches' coalescence induced the clogging of holes on the surface (Figs. 5c,d). The variation in the morphology and porous structure is attributed to the manipulation of the growth kinetics by adjusting the molar ratio $[Ba^{2+}]/[\ Mo_7O_{24}{}^{6-}]$.

The change of hydrophobic imidazolium substituent alkyl chain length gives us another important method for the modulation of crystal growth. When [Bmim]TA was used as direction reagent rather than [Omim]TA, i.e., the imidazolium substituent alkyl chain length was decreased, the morphology of $BaMoO_4$ was still dendritic structure. Compared with the results shown in Fig. 3, Fig. 6 shows that the size of the long central stem and branches was decreased and the microtower structure of branch was not clear. The building blocks assembling into the hierarchical architectures are also truncated octahedron.

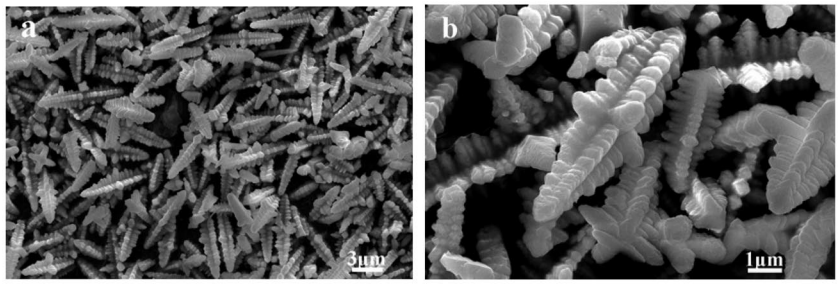

Fig. 6 SEM images of the $BaMoO_4$ dendritic crystals synthesized at 70 °C for 20 min under microwave irradiation in the presence of [Bmim]TA aqueous solution, which the concentration of initial reagents $[Ba^{2+}] = [Mo_7O_{24}{}^{6-}] = 0.02$ M and the molar ratio $[Ba^{2+}]/[Mo_7O_{24}{}^{6-}] = 1$.

Uniform shuttle-like $BaMoO_4$ crystals were also obtained (Fig. 7) when $[C_{16}mim]TA$ was used as direction reagents. Compared to the products synthesized in [Bmim]TA or [Omim]TA, the product synthesized in $[C_{16}mim]TA$ displayed a similar outline with the dendritic structure, however, the building blocks become the nanosheets (Fig. 7c) rather than truncated octahedron (Fig. 3e). Figure 7c indicates that these shuttle-like $BaMoO_4$ crystals were formed from stacking of nanosheets with a uniform thickness of about 50 nm. From the image of the tip of shuttle-like $BaMoO_4$ crystals (Fig. 7d), helical growth features are observed. Insets 1 and 2 of Fig. 7e are the low-magnification TEM images of the shuttle-like $BaMoO_4$ crystals, which are the lateral and tip view images, respectively. Inset 3 shows the SAED pattern recorded from the rim part of the shuttle-like $BaMoO_4$ crystals shown in inset 2. The SAED pattern confirms its single-crystalline structure with tetragonal symmetry. The SAED of this part should be attributed to the [001] zone, i.e., the plane that owns the largest area is the (002) plane. $BaXO_4$

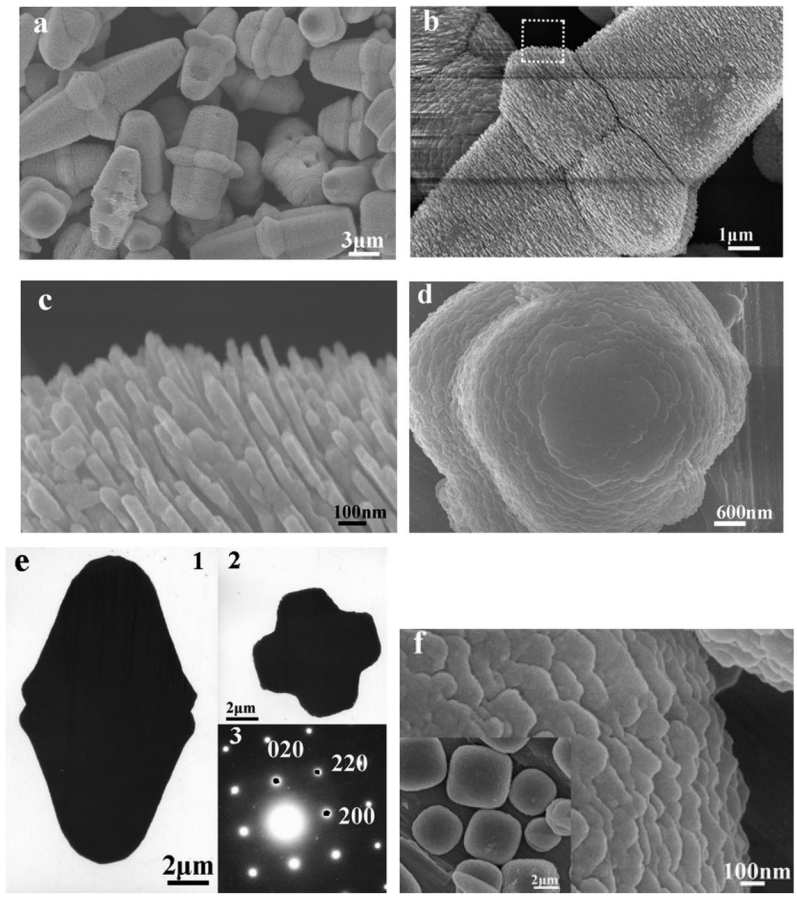

Fig. 7 SEM and TEM images of the $BaMoO_4$ shuttle-like crystals synthesized at 70 °C for 20 min under microwave irradiation in the presence of 1 g of $[C_{16}mim]TA$ aqueous solution, which the concentration of initial reagents $[Ba^{2+}] = [Mo_7O_{24}{}^{6-}] = 0.02$ M and the molar ratio $[Ba^{2+}]/[Mo_7O_{24}{}^{6-}] = 1$. (a) The low-magnification SEM image $BaMoO_4$ shuttle-like crystals; (b) SEM image of an individual $BaMoO_4$ shuttle-like crystal; (c) Enlarged image of the pane in (b); (d) Top view SEM image of individual $BaMoO_4$ shuttle-like crystal; (e) Insets 1 and 2 are the lateral TEM image and the top TEM image, respectively; insets 3 are the SAED pattern recorded from the rim part of the shuttle-like $BaMoO_4$ crystals shown in inset 2. (f) SEM images of the $BaMoO_4$ nanosheets synthesized at 70 °C for 20 min under microwave irradiation in the presence of 1 g of $[C_{16}mim]Br$ aqueous solution, which the concentration of initial reagents $[Ba^{2+}] = [Mo_7O_{24}{}^{6-}] = 0.02$ M. Inset is a low-magnification image.

(X = Mo, W) by itself tends to grow into shuttle-like structures along the [001] orientation (*c*-axis) [32,34]. The crystal growth along the [001] orientation is inhibited and force the crystal to grow into nanosheets in the presence of $[C_{16}mim]TA$. It is obvious that the long hydrophobic imidazolium substituent alkyl chain should be responsible for the formation of the nanosheet. With the increase of imidazolium substituent alkyl chain length, the building blocks become from the truncated octahedron to the nanosheet, i.e., the long alkyl chain exhibits a strong inhibiting effect on the crystal growth. $[C_{16}mim]Br$ containing anion Br^- was also employed to synthesize the $BaMoO_4$ crystal. $BaMoO_4$ spherical nanostructure consisting of numbers of nanosheets have been obtained by using $[C_{16}mim]Br$ as direction reagent (insert in Fig. 7f). From Fig. 7f, it is obvious that these spherical nanostructures were formed from the stacking of nanosheets. Therefore, it can be concluded that the functional anion CF_3COO^- plays a crucial role in the formation of shuttle-like $BaMoO_4$ crystals. The influences that functionalized cations and anions exert on the formation of $BaMoO_4$ crystals are summarized in Scheme 2.

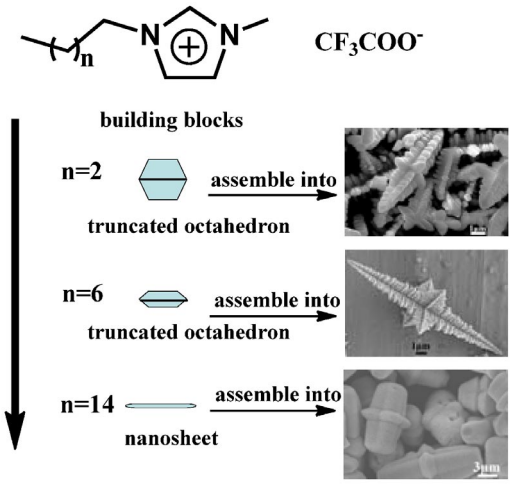

Scheme 2 Schematic illustration of the influences that functionalized cations and anions exert on the formation of $BaMoO_4$ crystals.

In order to emphasize the importance of $[C_{16}mim]TA$ in the formation of well-defined hierarchical structures, a series of comparative experiments was carried out through similar processes. It is obvious that the amount of $[C_{16}mim]TA$ in the solution profoundly affect the morphology and size of the as-obtained products. When the amount of $[C_{16}mim]TA$ was 0.1 g and the other experimental conditions were unchanged, large numbers of nanosheets were obtained and shown in Fig. 8a. The left inset in Fig. 8a shows that these cracked nanosheets are about 30 nm in thickness. Several hexagonal nanosheets with lesser size are also observed in the right inset in Fig. 8a. It is reasonable to conclude that these nanosheets are hexagon, however, the large size and thin thickness inducing these nanosheets are fragile. When the concentrations of initial reagents were increased to 0.1 M, hexagonal microsheets were obtained (Fig. 8b). The inset in Fig. 8b shows that the hexagonal microsheets are about 800 nm in thickness. With the amount of $[C_{16}mim]TA$ increased to 0.3 g, the stacking of several nanosheets was observed in Fig. 8c and the stacking of nanosheets should originate from the helical growth of the nanosheets. The helical growth features are observed on many nanosheets (insert in Fig. 8c) and the helical growth features are similar with the result shown in Fig. 7d. When the amount of $[C_{16}mim]TA$ increased to 0.5 g, it is observed that many nanosheets have been stacked. The amount of nanosheets con-

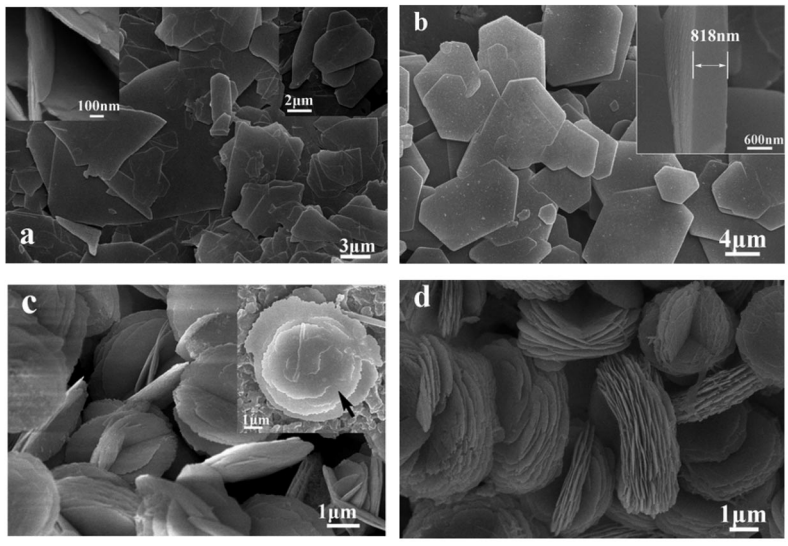

Fig. 8 (a) SEM images of the $BaMoO_4$ nanosheets synthesized at 70 °C for 20 min under microwave irradiation in the presence of 0.1 g of $[C_{16}mim]TA$ aqueous solution, which the concentration of initial reagents $[Ba^{2+}] = [Mo_7O_{24}^{6-}] = 0.02$ M. (b) SEM image of the $BaMoO_4$ microsheets synthesized at the concentration of initial reagents $[Ba^{2+}] = [Mo_7O_{24}^{6-}] = 0.1$ M and other reaction parameter are same as the Fig. 8a; (c) SEM images of the $BaMoO_4$ nanosheets synthesized in the presence of 0.3 g of $[C_{16}mim]TA$ aqueous solution and other reaction parameter are same as the Fig. 8a, the inset is the individual nanosheets SEM image; (d) SEM images of the $BaMoO_4$ nanosheets synthesized in the presence of 0.5 g of $[C_{16}mim]TA$ aqueous solution and other reaction parameter are same as the Fig. 8a.

nected together are more than that prepared in 0.3 g $[C_{16}mim]TA$. These results imply that the greater the amount of $[C_{16}mim]TA$ added, the more nanosheets are connected together.

CONCLUSION

In summary, $BaMoO_4$ crystals with different morphologies have been successfully synthesized under the direction of functionalized ILs with different imidazolium substituent alkyl chain length. With the increase of the imidazolium substituent alkyl chain length, the inhibiting effect of hydrophobic alkyl chain has been obviously enhanced. Compared to the products synthesized in [Bmim]TA or [Omim]TA, the product synthesized in $[C_{16}mim]TA$ displayed similar shuttle-like outline with the dendritic structure. However, the building blocks become the nanosheets rather than microscale truncated octahedron. Single-crystalline $BaMoO_4$ with complex dendritic structure can be achieved through oriented attachment of nanoparticles under the direction of [Omim]TA. The controllable synthesis of $BaMoO_4$ porous structure is attributed to the manipulation of the growth kinetics by adjusting the molar ratio $[Ba^{2+}]/[Mo_7O_{24}^{6-}]$. These holes originated from the unfinished coalescence of branches of $BaMoO_4$ dendritic structure, which may provide another new viewpoint on the controllable synthesis of porous materials.

ACKNOWLEDGMENTS

The authors extend special thanks to Weidong Zhou, Qingli Huang, and Bin Xu (Analysis Center, Yangzhou University) for kindly supporting FESEM and XRD measurements. The present work is sup-

ported by the National Natural Science Foundation of China (Grants No. 20676057, 20876071, and 20875039) and Doctoral Innovation Fund of Jiangsu (CX08B-142Z).

REFERENCES

1. S. J. Chen, Y. C. Liu, C. L. Shao, R. Mu, Y. M. Lu, J. Y. Zhang, D. Z. Shen, X. W. Fan. *Adv. Mater*. **17**, 586 (2005).
2. A. K. Ganguli, T. Ahmad, S. Vaidya, J. Ahmed. *Pure Appl. Chem.* **80**, 2451 (2008).
3. Q. Zhou, S. Wang, N. Q. Jia, L. Liu, J. J. Yang, Z. Y. Jiang. *Mater. Lett.* **60**, 3789 (2006).
4. F. Kim, S. Kwan, J. Akana, P. D. Yang. *J. Am. Chem. Soc*. **123**, 4360 (2001).
5. H. B. Zeng, P. S. Liu, W. P. Cai, X. L. Cao, S. K. Yang. *Cryst. Growth Des*. **7**, 1092 (2007).
6. Z. C. Wu, C. Pan, Z. Y. Yao, Q. R. Zhao, Y. Xie. *Cryst. Growth Des*. **6**, 1717 (2006).
7. X. Y. Chen, X. Wang, Z. H. Wang, X. G. Yang, Y. T. Qian. *Cryst. Growth Des*. **5**, 347 (2005).
8. G. J. Zhou, M. K. Lü, Z. L. Xiu, S. F. Wang, H. P. Zhang, Y. Y. Zhou, S. M. Wang. *J. Phys. Chem. B* **110**, 6543 (2006).
9. P. Badica. *Cryst. Growth Des*. **7**, 794 (2007).
10. S. M. Lee, Y. W. Jun, S. N. Cho, J. W. Cheon. *J. Am. Chem. Soc*. **124**, 11244 (2002).
11. E. J. H. Lee, C. Ribeiro, E. Longo, E. R. Leite. *J. Phys. Chem. B* **109**, 20842 (2005).
12. Y. Wang, Q. S. Zhu, H. G. Zhang. *Chem. Commun*. 5231 (2005).
13. Y. Cheng, Y. S. Wang, D. Q. Chen, F. Bao. *J. Phys. Chem. B* **109**, 794 (2005).
14. Q. Y. Lu, F. Gao, S. Komarneni. *J. Am. Chem. Soc*. **126**, 54 (2004).
15. Q. Gong, X. F. Qian, H. L. Cao, W. M. Du, X. D. Ma, M. S. Mo. *J. Phys. Chem. B* **110**, 19295 (2006).
16. M. Antonietti, D. B. Kuang, B. Smarsly, Y. Zhou. *Angew. Chem., Int. Ed.* **43**, 4988 (2004).
17. H. Itoh, K. Naka, Y. Chujo. *J. Am. Chem. Soc*. **126**, 3026 (2004).
18. Z. H. Li, Z. M. Liu, J. L. Zhang, B. X. Han, J. M. Du, Y. N. Gao, T. Jiang. *J. Phys. Chem. B* **109**, 14445 (2005).
19. Y. Wang, H. Yang. *J. Am. Chem. Soc*. **127**, 5316 (2005).
20. H. G. Zhu, J. F. Huang, Z. W. Pan, S. Dai. *Chem. Mater.* **18**, 4473 (2006).
21. K. Yoo, H. Choi, D. D. Dionysiou. *Chem. Commun*. 2000 (2004).
22. Y. Jiang, Y. J. Zhu. *J. Phys. Chem. B* **109**, 4361 (2005).
23. J. Jiang, S. H. Yu, W. T. Yao, H. Ge, G. Z. Zhang. *Chem. Mater.* **17**, 6094 (2005).
24. W. W. Wang, Y. J. Zhu. *Cryst. Growth Des*. **5**, 505 (2005).
25. A. P. A. Marques, D. M. A. D. Melo, E. Longo, C. A. Paskocimas, P. S. Pizani, E. R. Leite. *J. Solid State Chem.* **178**, 2346 (2005).
26. W. S. Cho, M. Yoshimura. *Solid State Ionics* **100**, 143 (1997).
27. C. Zhang, E. H. Shen, E. B. Wang, Z. H. Kang, L. Gao. C. W. Hu, L. Xu. *Mater. Chem. Phys.* **96**, 240 (2006).
28. P. Yang, G. Q. Yao, J. H. Lin. *Inorg. Chem. Commun.* **7**, 389 (2004).
29. Y. Ding, S. H. Yu, C. Liu, Z. A. Zang. *Chem.—Eur. J.* **13**, 746 (2007).
30. Z. H. Li, J. M. Du, J. L. Zhang, T. C. Mu, Y. N. Gao, B. X. Han, J. Chen, J. W. Chen. *Mater. Lett*. **59**, 64 (2005).
31. A. P. D. A. Marques, D. M. A. D. Melo, C. A. Paskocimas, P. S. Pizani, M. R. Joya, E. R. Leite, E. Longo. *J. Solid State Chem*. **179**, 671 (2006).
32. H. T. Shi, L. M. Qi, J. M. Ma, N. Z. Wu. *Adv. Funct. Mater.* **15**, 442 (2005).
33. H. T. Shi, X. H. Wang, N. N. Zhao, L. M. Qi, J. M. Ma. *J. Phys. Chem. B* **110**, 748 (2006).
34. Z. J. Luo, H. M. Li, H. M. Shu, K. Wang, J. X. Xia, Y. S. Yan. *Cryst. Growth Des*. **8**, 2275 (2008).
35. Z. J. Luo, H. M. Li, H. M. Shu, K. Wang, J. X. Xia, Y. S. Yan. *Mater. Chem. Phys.* **110**, 17 (2008).
36. Y. Jiang, Y. J. Zhu, G. F. Cheng. *Cryst. Growth Des.* **6**, 2174 (2006).
37. Z. F. Fei, T. J. Geldbach, D. B. Zhao, P. J. Dyson. *Chem.—Eur. J.* **12**, 2122 (2006).

38. P. Bonhôte, A. P. Dias, N. Papageorgiou, K. Kalyanasundaram, M. Grätzel. *Inorg. Chem.* **35**, 1168 (1996).